Inorganic Chemistry

Article

pubs.acs.org/IC

Crystal and Electronic Structure and Magnetic Properties of Divalent Europium Perovskite Oxides EuMO_3 (M = Ti, Zr, and Hf): Experimental and First-Principles Approaches

Hirofumi Akamatsu,*[,†] Koji Fujita,*[,‡] Hiroyuki Hayashi,[†] Takahiro Kawamoto,[‡] Yu Kumagai,[†] Yanhua Zong,[‡] Koji Iwata,[‡] Fumiyasu Oba,[†] Isao Tanaka,[†] and Katsuhisa Tanaka[‡]

[†]Department of Materials Science and Engineering, Graduate School of Engineering, Kyoto University, Sakyo, Kyoto 606-8501, Japan

[‡]Department of Material Chemistry, Graduate School of Engineering, Kyoto University, Nishikyo, Kyoto 615-8510, Japan

ABSTRACT: A comparative study of the crystal and electronic structure and magnetism of divalent europium perovskite oxides EuMO_3 (M = Ti, Zr, and Hf) has been performed on the basis of both experimental and theoretical approaches playing complementary roles. The compounds were synthesized via solid-state reactions. $EuZrO_3$ and $EuHfO_3$ have an orthorhombic structure with a space group *Pbnm* at room temperature contrary to $EuTiO_3$, which is cubic at room temperature. The optical band gaps of $EuZrO_3$ and $EuHfO_3$ are found to be about 2.4 and 2.7 eV, respectively, much larger than that of $EuTiO_3$ (0.8 eV). On the other hand, the present compounds exhibit similar magnetic properties characterized by paramagnetic-antiferromagnetic transitions at around 5 K, spin flop at moderate magnetic fields lower than 1 T, and the antiferromagnetic nearest-neighbor and ferromagnetic next-nearest-neighbor exchange interactions. First-principles calculations based on a hybrid Hartree−Fock density functional approach yield lattice constants, band gaps, and magnetic interactions in good agreement with those obtained experimentally. The band gap excitations are assigned to electronic transitions from the Eu 4f to M *n*d states for EuMO_3 (M = Ti, Zr, and Hf and n = 3, 4, and 5, respectively).

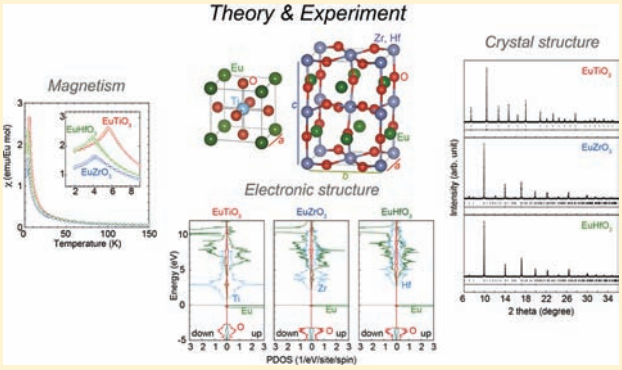

INTRODUCTION

Divalent europium perovskite oxides with a chemical formula EuMO_3 (M = Ti and Zr) and the related solid solutions exhibit diverse and intriguing physical properties, rendering them subjects of great interest. Magnetic properties of the compounds and their correlation with dielectric and carrier-transport properties such as magnetoelectric effects and anomalous Hall effects have been extensively investigated by means of both experimental and theoretical methods.[1−10] In addition, these compounds have been synthesized via various methods in the form of single crystals,[2,3] polycrystals,[11−15] nanocrystals,[16] and epitaxial thin films.[6,17−21]

$EuTiO_3$ has a cubic perovskite structure (space group $Pm\bar{3}m$) with a lattice constant of 3.9 Å at room temperature[11] (see Figure 1a), and, therefore, is isostructural to $SrTiO_3$. It is an insulator with a band gap of 1 eV,[16,18] and exhibits incipient ferroelectric behavior.[3] The localized 4f spins belonging to the A-site Eu^{2+} ions (S = 7/2) compose a simple cubic lattice with a G-type antiferromagnetic (AFM) ordering below 5.3 K.[23] Interestingly, first-principles calculations have revealed that $EuTiO_3$ is critically balanced between the AFM and ferromagnetic (FM) states.[5,24,25] Our recent calculations have demonstrated that this criticality is caused by competition between AFM superexchange via the Ti 3d states and FM indirect exchange through the Eu 5d bands proposed by Goodenough[26] and Kasuya[27] in the nearest-neighbor (NN) interaction.[28] The importance of the superexchange between Eu 4f spins via the Ti 3d states stems from the electronic structure unique to $EuTiO_3$, because the energy gap between the Ti 3d and the Eu 4f states corresponding to the band gap is

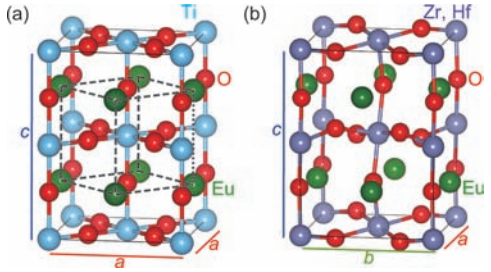

Figure 1. Schematic models of (a) a $\sqrt{2} \times \sqrt{2} \times 2$ tetragonal supercell for $EuTiO_3$ and (b) an orthorhombic unit cell with a space group of *Pbnm* for EuMO_3 (M = Zr and Hf). The broken lines in (a) indicate the cubic unit cell with a space group of $Pm\bar{3}m$. The crystal structures are visualized using the VESTA code.[22]

Received: November 14, 2011
Published: April 2, 2012

   dx.doi.org/10.1021/ic2024567 | *Inorg. Chem.* 2012, 51, 4560−4567

relatively small (~1 eV).[16,18] The delicate balance between the AFM and FM states implies that the magnetic ground state in $EuTiO_3$ can be altered by some perturbations. For example, $EuTiO_3$ is transformed from an AFM insulator to a FM metal by electronic-carrier doping of Ti 3d bands,[2] and it is changed into a reentrant ferromagnet by amorphization.[29] The observation of FM properties has been also reported for epitaxial $EuTiO_3$ thin films with out-of-plane lattice expansion[19] and biaxial tensile strain.[21] In particular, Lee et al.[21] have experimentally confirmed the theoretical prediction by Fennie and Rabe[5] that biaxial tensile strain induces a multiferroic (FM and ferroelectric) state.

In addition to $EuTiO_3$, $EuZrO_3$ and $EuHfO_3$ are involved in the divalent europium perovskites having Group 4 elements in the B sites. Recently, it has been reported that $EuZrO_3$ adopts an orthorhombic perovskite structure with a space group of *Pbnm* (see Figure 1b).[14,15] The Eu sites form a pseudosimple-cubic lattice and the Eu 4f spins have been suggested to exhibit a *G*-type AFM ordering below 4.1 K.[15] On the other hand, there are few reports about preparation and physical properties of $EuHfO_3$.[13] For systematic understanding of the magnetism in the divalent europium perovskites, the comparative investigations of their fundamental properties including the crystal and electronic structure will be helpful.

In this study, experimental approaches, in conjunction with theoretical calculations, have elucidated the crystal and electronic structure and magnetic properties of the divalent europium perovskite oxides, $EuMO_3$ (M = Ti, Zr, and Hf). The crystal structures, local environments, and chemical states of europium ions, optical band gaps, and magnetizations are investigated for polycrystalline $EuMO_3$ (M = Ti, Zr, and Hf) using synchrotron X-ray diffraction (XRD), ^{151}Eu Mössbauer spectroscopy, diffuse reflectance spectroscopy, and a superconducting quantum interference device (SQUID) magnetometer, respectively. First-principles calculations based on a hybrid Hartree–Fock density functional approach provide lattice constants, magnetic ground states, and band gaps, in good agreement with those obtained experimentally and also specify the nature of the electronic transition corresponding to the band gap excitation. The complementary study via both experimental and theoretical approaches systematically clarifies the fundamental properties of the divalent europium perovskites.

EXPERIMENTAL SECTION

Sample Preparation. Polycrystalline $EuMO_3$ (M = Ti, Zr, and Hf) samples were prepared via a solid-state reaction from reagent-grade Eu_2O_3, TiO_2, ZrO_2, and HfO_2. For $EuTiO_3$, Eu_2O_3 and TiO_2 were thoroughly mixed and pressed into a pellet. Then, the resultant pellet was sintered at 1673 K for 12 h in air. The sintered body was pulverized and sintered at 1473 K in a reducing atmosphere of 95 vol. % Ar + 5 vol.% H_2. The black powder thus obtained was pelletized again, and then the reaction was completed by resintering at 1473 K for 24 h in the reducing atmosphere. For $EuMO_3$ (M = Zr and Hf) samples, the following two consecutive reactions were used for the preparation:[15] (1) $Eu_2O_3 + C \rightarrow CO + 2EuO$ and (2) $EuO + MO_2 \rightarrow EuMO_3$. In the first step, Eu_2O_3 and slightly excessive graphite acting as a reducing agent were thoroughly mixed and pressed into a pellet. The pellet was then sintered at 1723 K for 6 h in the reducing atmosphere. In the second step, the resultant EuO pellet was reground into powder and thoroughly mixed with MO_2 powder. The mixture was again pressed into a pellet and sintered at 1823 K for 6 h in the reducing atmosphere. The resultant pellet was greenish yellow.

Measurements of Structural, Optical, and Magnetic Properties. Powder XRD measurements were performed at room temperature using a Rigaku RINT 2500 system with Cu$K\alpha$ radiation to confirm whether single-phase samples were obtained or not. The crystal structure of the samples was determined by high-resolution synchrotron XRD patterns taken with a Debye–Scherrer camera at the BL02B2 beamline of SPring-8. Imaging plates were utilized as a detector. The wavelength of incident beam was estimated to be 0.49880 Å by calibration using CeO_2 as a standard. The RIETAN-FP was used for the structural refinement.[30] Energy dispersive spectroscopy revealed that the molar ratio of Eu to M (M = Ti, Zr, and Hf) was almost 1:1. ^{151}Eu Mössbauer transmission spectra were measured at room temperature using 1.85 GBq $^{151}Sm_2O_3$ as a 21.5 keV γ-ray source. The velocity calibration was done with the magnetic hyperfine spectrum of α-Fe foil obtained using a 14.4 keV γ-ray of ^{57}Co doped in Rh. The Mössbauer spectrum of EuF_3 was utilized as a standard for the isomer shift. To estimate optical band gaps, diffuse reflectance spectra were collected over a photon-energy range from 0.7 to 3.5 eV. Magnetic properties were measured by using a SQUID magnetometer (Quantum Design, model MPMS-XL).

COMPUTATIONAL SECTION

The first-principles hybrid Hartree–Fock density functional calculations were performed using the projector augmented-wave (PAW) method[31] and the HSE06 functional[32−34] as implemented in the VASP code.[35−39] The HSE06 functional adopts the replacement of one-quarter of the exchange energy in the Perdew–Burke–Ernzerhof generalized gradient approximation (PBE-GGA)[40] with the nonlocal Fock exchange, and a screening parameter of 0.208 Å^{-1}. It has been shown that the hybrid Hartree–Fock density functional approach describes the electronic structure for a variety of molecules and solids more precisely than those obtained from the local and semilocal functionals.[32−34,38,39,41−49]

The PAW data sets with radial cutoffs of 1.5, 1.2, 1.3, 1.4, and 0.8 Å for Eu, Ti, Zr, Hf, and O, respectively, were used with a plane-wave cutoff energy of 550 eV. Eu 4f, 5s, 5p, 6s; Ti 3s, 3p, 3d, 4s; Zr 4s, 4p, 4d, 5s; Hf 5p, 5d, 6s; and O 2s, 2p states were described as valence electrons.

The supercell was chosen to be so large as to extract the effective exchange constants for the NN and next-nearest-neighbor (NNN) exchange paths. To model four magnetic configurations, that is, *A*-, *C*-, *F*-, and *G*-type, a $\sqrt{2} \times \sqrt{2} \times 2$ tetragonal supercell containing 20 atoms shown in Figure 1a was used for $EuTiO_3$, and an orthorhombic unit cell possessing 20 atoms with a space group of *Pbnm* shown in Figure 1b was adopted for $EuZrO_3$ and $EuHfO_3$. Here, the four magnetic configurations mentioned above are defined for $EuZrO_3$ and $EuHfO_3$ by regarding the lattice composed of Eu^{2+} ions as simple cubic. A $3 \times 3 \times 2$ k-point mesh was used for both cells in accordance with the Monkhorst-Pack scheme.[50] The lattice constants and internal coordinates were optimized until the residual stress and force converged to less than 0.2 GPa and 0.02 eV/Å, respectively. The NN and NNN exchange constants were calculated by mapping the total energy difference among the four magnetic configurations onto the Heisenberg Hamiltonian. The method to estimate the exchange constants was described in detail in our previous report.[28]

RESULTS AND DISCUSSION

Crystal Structure. Figure 2 shows room-temperature synchrotron XRD profiles of $EuMO_3$ (M = Ti, Zr, and Hf) and the results of fitting by Rietveld analysis. The XRD pattern of $EuTiO_3$ is readily indexed on the basis of the cubic unit cell as illustrated by the broken lines in Figure 1a, while the patterns of $EuZrO_3$ and $EuHfO_3$ are assigned to the orthorhombic unit cell shown in Figure 1b. The Rietveld refinement (solid curves in Figure 2) was performed based on the space group $Pm\bar{3}m$ (No. 221) for $EuTiO_3$ and *Pbnm* (No. 62) for $EuMO_3$ (M = Zr and Hf). Since no apparent vacancy was observed at any sites, the occupancy factors were constrained to unity. The resultant structural parameters are shown in Table 1. The small values of the reliability factors (R_{wp} and R_p) and goodness-of-fit (S_{fit})

dx.doi.org/10.1021/ic2024567 | Inorg. Chem. 2012, 51, 4560−4567

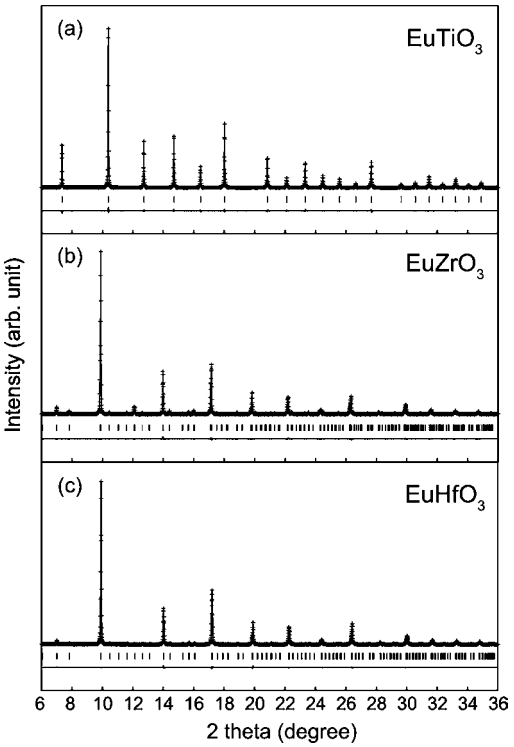

Figure 2. Synchrotron X-ray diffraction profiles measured at room temperature (crosses) and calculated profiles obtained by Rietveld analysis (solid curves) for (a) $EuTiO_3$, (b) $EuZrO_3$, and (c) $EuHfO_3$. The vertical ticks indicate the positions of the Bragg reflections, and the bottom solid lines correspond to the difference between the observed and the calculated intensity.

indicate the verification of the refinement based on the above structural models. The values of atomic displacement parameters U for the Eu ions are relatively large, partly because of the presence of a small amount of Eu^{3+} ions in the A site (<5 mol %) as mentioned in the next section.

The lattice constant of $EuTiO_3$ is in good agreement with that reported for single crystalline and polycrystalline bulk samples.[3,11,51] The lattice constants and atomic coordinates of $EuZrO_3$ are also very similar to those reported in refs 14 and 15. It is well-known that $EuTiO_3$ is isostructural to $SrTiO_3$ at room temperature. Similarly, the structural parameters of $EuZrO_3$ and $EuHfO_3$ are similar to those of $SrZrO_3$[52] and $SrHfO_3$,[53] respectively. If the crystal structure with the *Pbnm* symmetry is regarded as a pseudocubic structure, we can define the pseudocubic lattice constant as $a_{pc} = (abc/4)^{1/3}$, where a, b, and c are lattice constants for the orthorhombic unit cell. The relationship among the lattice constant of $EuTiO_3$ (3.90437 Å) and the pseudocubic lattice constants of $EuZrO_3$ (4.10371 Å) and $EuHfO_3$ (4.08849 Å) are accounted for in terms of the ionic radii[54] of Ti^{4+} (0.61 Å), Zr^{4+} (0.72 Å), and Hf^{4+} (0.71 Å) for octahedral coordinations. The difference between the $Pm\bar{3}m$ and *Pbnm* structures is well characterized by rotations of MO_6 octahedra; the $Pm\bar{3}m$ and *Pbnm* structures are represented by $a^0a^0a^0$ and $a^-a^-c^+$, respectively, with Glazer notation.[55] The rotation arises when the ionic radii of the A-site cations are too small to fully occupy the interstitial volume of the MO_6 network. The ZrO_6 and HfO_6 octahedra, which are considerably larger than the TiO_6 octahedra, rotate so as to reduce the available volume of Eu^{2+} ions. Bond valence sum (BVS) calculations provide (Eu, Ti) = (2.28, 4.14) for $EuTiO_3$, (Eu, Zr) = (2.00, 3.96) for $EuZrO_3$, and (Eu, Hf) = (2.02, 3.93) for $EuHfO_3$, indicating that the ionic composition $Eu^{2+}M^{4+}O_3$ (M = Ti, Zr, and Hf) is plausible. For $EuTiO_3$, the slight discrepancy of BVS from the formal charges $Eu^{2+}Ti^{4+}O_3$ may be related to an antiferrodistortive phase transition into a structure with lower symmetry, which has been recently suggested by a specific-heat measurement to occur at 282 K, slightly lower than room temperature.[56,57] It is naturally anticipated that $EuTiO_3$ undergoes such a transition at lower temperatures because isostructural $SrTiO_3$ exhibits an antiferrodistortive structure ($a^0a^0c^-$) distortion below 105 K.[58] Our preliminary analysis of variable-temperature powder XRD data of $EuTiO_3$ supports the presence of the antiferrodistortive transition below room temperature, the detail of which will be described elsewhere.

Local Structure of Europium Ions. Figure 3 illustrates the ^{151}Eu Mössbauer spectra at room temperature for the present compounds. Each of the spectra is composed of an intense absorption peak due to Eu^{2+} at −14 ∼ −12 mm/s and a weak absorption peak due to Eu^{3+} at 0∼1 mm/s. It is found from the

Table 1. Refined Structural Parameters for $EuMO_3$ with M = Ti, Zr, and Hf

atom	site	g	x	y	z	$1000U$ (Å^2)
			$EuTiO_3$[a]			
Eu	1b	1	$^1/_2$	$^1/_2$	$^1/_2$	6.2(1)
Ti	1a	1	0	0	0	3.2(2)
O	3d	1	$^1/_2$	0	0	7.6(3)
			$EuZrO_3$[b]			
Eu	4c	1	0.0065(2)	0.5262(1)	$^1/_4$	7.7(2)
Zr	4a	1	0	0	0	1.8(2)
O1	4c	1	−0.0626(12)	−0.0169(8)	$^1/_4$	6.5(9)
O2	8d	1	0.2222(11)	0.2804(9)	0.0418(6)	6.5(9)
			$EuHfO_3$[c]			
Eu	4c	1	0.0056(3)	0.5226(1)	$^1/_4$	7.2(2)
Hf	4a	1	0	0	0	2.6(1)
O1	4c	1	−0.0630(18)	−0.0135(12)	$^1/_4$	2.3(13)
O2	8d	1	0.2289(16)	0.2779(13)	0.0414(9)	2.3(13)

[a]$EuTiO_3$: Space group $Pm\bar{3}m$ (No. 221), lattice constants: a = 3.90437(4) Å, R_{wp} = 4.27%, R_p = 3.29%, and S_{fit} = 1.41. [b]$EuZrO_3$: Space group *Pbnm* (No. 62), lattice constants: a = 5.79387(10) Å, b = 5.82154(9) Å, and c = 8.19562(14) Å, R_{wp} = 1.95%, R_p = 1.32%, and S_{fit} = 0.85. [c]$EuHfO_3$: Space group *Pbnm* (No. 62), lattice constants: a = 5.77869(12) Å, b = 5.79424(12) Å, and c = 8.16438(17) Å, R_{wp} = 4.32%, R_p = 2.98%, and S_{fit} = 0.82.

dx.doi.org/10.1021/ic2024567 | Inorg. Chem. 2012, 51, 4560−4567

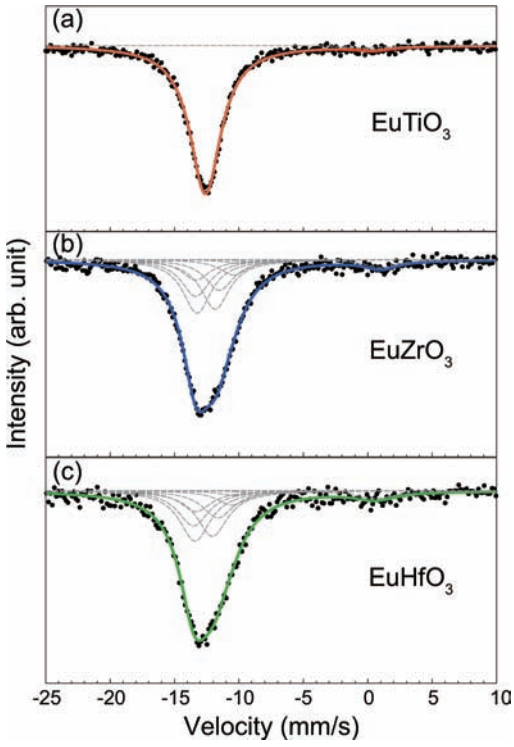

Figure 3. ^{151}Eu Mössbauer spectra (dots) measured at room temperature for (a) $EuTiO_3$, (b) $EuZrO_3$, and (c) $EuHfO_3$. The solid curves represent the theoretical spectra. The dashed curves depict the 12 component curves for the Eu^{2+} absorption peak at around −13 mm/s and the Eu^{3+} absorption line at around 0 mm/s.

area ratio of the two absorption peaks that most of the europium ions are present as Eu^{2+} ions in the present samples (see Table 2). The Eu^{2+} absorption line for $EuTiO_3$ manifests a

Table 2. ^{151}Eu Mössbauer Parameters for EuMO_3 (M = Ti, Zr, and Hf) Obtained by the Fit of Theoretical Curves to the Experimental Spectra in Figure 3[a]

notation	$A_{Eu^{2+}}/A_{Eu}$	δ[b] (mm/s)	eQV_{zz}[c] (mm/s)	η[d]	γ[e] (mm/s)
$EuTiO_3$	0.97	−12.60(1)			2.92(4)
$EuZrO_3$	0.96	−12.39(2)	−10.2(3)	0.44(6)	2.70(7)
$EuHfO_3$	0.95	−12.55(3)	−10.2(5)	0.32(13)	2.90(12)

[a]The area ratio of the Eu^{2+} absorption relative to the total absorption, $A_{Eu^{2+}}/A_{Eu}$, is also shown. [b]δ: isomer shift relative to EuF_3. [c]eQV_{zz}: quadrupole interaction parameter. [d]η: asymmetry parameter. [e]γ: full width at half-maximum of one component of Lorentzian multiples.

symmetric shape, which reflects the cubic symmetry at the Eu^{2+} site in $EuTiO_3$. The fitting of a single Lorentzian function to the Eu^{2+} and Eu^{3+} absorption lines did well for $EuTiO_3$ (see Figure 3a). The isomer shift, δ, and full width at half-maximum, γ, for the Eu^{2+} absorption line are shown in Table 2. In contrast, the Eu^{2+} absorption lines for $EuZrO_3$ and $EuHfO_3$ are slightly asymmetric and broader than that for $EuTiO_3$ because there is nonzero quadrupole splitting due to the lower symmetry at the Eu^{2+} site. The Eu^{2+} absorption lines for $EuZrO_3$ and $EuHfO_3$ were not fitted well using a single Lorentzian function. Therefore, taking into account quadrupole interactions, the Eu^{2+} absorption lines were analyzed using a method developed by Shenoy and Dunlap.[59] The detailed procedure for the analysis was described elsewhere.[60,61] The fitting curves are shown as solid lines in Figure 3b and c; the Eu^{2+} absorption line was fitted well with multiplet components of Lorentzian functions corresponding to 12 possible transitions due to the quadrupole interactions, while the Eu^{3+} absorption lines were analyzed using a single Lorentzian function because of the poor spectral resolution. Table 2 lists the fitting parameters including δ, γ (for a single Lorentzian function), eQV_{zz}, and $\eta = (V_{xx} - V_{yy})/V_{zz}$, where e is the elementary electronic charge, $V_{\sigma\sigma}$ is the electric-field gradient in the σ axis, and Q is the nuclear quadrupole moment at the ground state.

The δ values are about −12.5 mm/s for the present compounds. The δ value of $EuTiO_3$ is slightly lower than those of $EuZrO_3$ and $EuHfO_3$. In $EuTiO_3$, an Eu ion has 12 equivalent Eu−O bonds for the NN O ions. On the other hand, because of the lowering of symmetry, the oxygen coordination number of Eu ion is effectively decreased. These values are similar to those reported for the Eu^{2+} perovskites[15,51,62] and melilites[63] where the Eu^{2+} ions are present at the 12-fold- and 8-fold-coordinated sites, respectively.

Band Gap. Diffuse reflectance spectra measured at room temperature are shown in Figure 4 for EuMO_3 with M = Ti, Zr,

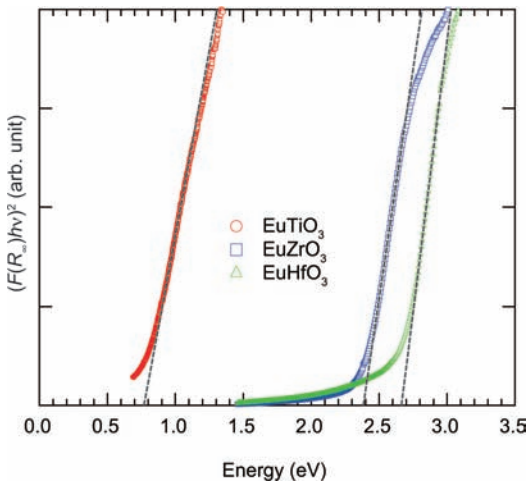

Figure 4. Diffuse reflectance spectra for EuMO_3 with M = Ti (red), Zr (blue), and Hf (green) at room temperature. Plots of $(F(R_\infty)h\nu)^2$ vs photon energy are shown. Band gaps are indicated by the energy intercepts of the broken lines.

and Hf. The absorption coefficient, α, is obtained from the Kubelka−Munk (K-M) function defined as

$$F(R_\infty) = \frac{\alpha}{S} = \frac{(1 - R_\infty)^2}{2R_\infty} \quad (1)$$

where R_∞ is the reflectance and S is the scattering coefficient. The photon-energy ($h\nu$) dependence of α for the direct allowed transition obeys the following equation:

$$\alpha = A\frac{(h\nu - E_g)^{1/2}}{h\nu} \quad (2)$$

where A is a constant and E_g is the band gap. The diffuse reflectance spectra of EuMO_3 (M = Ti, Zr, and Hf) were analyzed using eq 2. This is because the calculated band structures for these compounds indicate the predominance of direct allowed transitions as mentioned below. Figure 4 presents $(F(R_\infty)h\nu)^2$ as a function of $h\nu$. The photon-energy intercept of the linear portion of $h\nu$ variation of $(F(R_\infty)h\nu)^2$

dx.doi.org/10.1021/ic2024567 | Inorg. Chem. 2012, 51, 4560−4567

yields E_g = 0.8, 2.4, and 2.7 eV for $EuTiO_3$, $EuZrO_3$, and $EuHfO_3$, respectively. The E_g value for $EuTiO_3$ is in good agreement with those obtained by absorption spectroscopy for an epitaxial thin film on a $SrTiO_3$ substrate[18] and nanoparticles.[16] The E_g values for $EuZrO_3$ and $EuHfO_3$ are comparable to each other and significantly larger than that for $EuTiO_3$.

Magnetic Properties. The temperature dependence of magnetic susceptibility $\chi(T)$ and its reciprocal $\chi^{-1}(T)$ for $EuMO_3$ (M = Ti, Zr, and Hf) is displayed in Figure 5a and b,

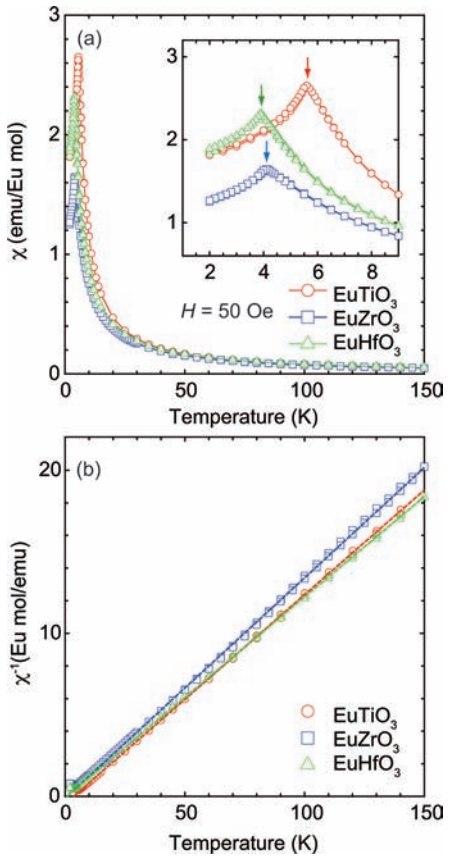

Figure 5. Temperature dependence of (a) magnetic susceptibility and (b) its reciprocal measured under a magnetic field of 50 Oe for $EuMO_3$ with M = Ti (red), Zr (green), and Hf (blue). The inset of (a) displays the enlarged view of the low-temperature region.

respectively. Both zero-field-cooling (ZFC) and field-cooling (FC) processes were carried out under a magnetic field of 50 Oe. The $\chi(T)$ curve for the ZFC process coincides with that for the FC process within experimental errors. Figure 5b reveals that the present compounds are Curie–Weiss paramagnetic (PM) at high temperatures. A kink structure at about 5 K in each of the $\chi(T)$ curves (see the inset of Figure 5a) indicates an PM to AFM transition at the Néel temperature. The $\chi^{-1}(T)$ curves at high temperatures were fitted by the following Curie–Weiss equation:

$$\chi^{-1}(T) = \frac{3k_B(T - \theta_W)}{N_A M_B^2 \mu_B^2} \quad (3)$$

where θ_W is the Weiss temperature, N_A the Avogadro constant, μ_B the Bohr magneton, M_B the effective number of Bohr magnetons, and k_B the Boltzmann constant. The values of θ_W and M_B obtained by the fitting are summarized in Table 3,

Table 3. Néel Temperature (T_N), Weiss Temperature (θ_W), and Effective Number of Bohr Magnetons (M_B) of $EuMO_3$ (M = Ti, Zr, and Hf)

	T_N (K)	θ_W (K)	M_B
$EuTiO_3$	5.5	3.6	7.9
$EuZrO_3$	4.1	0.85	7.5
$EuHfO_3$	3.9	0.74	8.2

together with the Néel temperature. The present compounds have positive values of θ_W in contrast to usual antiferromagnets.

As discussed later, the hybrid functional calculations show that the G-type AFM configuration is the most stable among the A-, C-, F-, and G-type magnetic configurations: it has been actually demonstrated by the neutron diffraction that low-temperature magnetic structure is G-type AFM for $EuTiO_3$.[23] Here, assuming that the present compounds exhibit the collinear G-type AFM ordering at low temperature, and taking into account only the NN and NNN exchange interactions, T_N and θ_W are represented on the basis of the molecular-field theory:

$$T_N = \frac{2S(S+1)}{3k_B}(-6J_1 + 12J_2) \quad (4)$$

$$\theta_W = \frac{2S(S+1)}{3k_B}(6J_1 + 12J_2) \quad (5)$$

where J_1 and J_2 are the mean NN and NNN exchange constants, respectively. Substituting T_N and θ_W derived from the $\chi(T)$ curves into eq 4 and eq 5, respectively, yields (J_1/k_B, J_2/k_B) = (−0.015 K, +0.036 K) for $EuTiO_3$, (J_1/k_B, J_2/k_B) = (−0.026 K, +0.020 K) for $EuZrO_3$, and (J_1/k_B, J_2/k_B) = (−0.025 K, +0.018 K) for $EuHfO_3$. The NN and NNN exchange interactions are AFM and FM, respectively, for all the present oxides.

Figure 6 illustrates the isothermal magnetization $M(H)$ at 2 K as a function of external magnetic field. At H of about 20000 Oe, $M(H)$ curves tend to be saturated, reaching about 7 μ_B per one formula unit. The saturation of magnetization at relatively small H is attributed to the small values of J_1, that is, the weak magnetic interaction between the sublattice magnetizations. A close look at Figure 6b reveals the spin-flop behavior at H of 5000 to 8000 Oe depending on the kind of M; in a low-field region, the slope of $M(H)$, $dM(H)/dH$, increases with an increase in H, and then becomes constant at the spin-flop field where the AFM components reorient perpendicular to the magnetic field. When H is applied to an antiferromagnet with uniaxial magnetic anisotropy at 0 K, a spin-flop field is represented as $H_c = (2K_uA_{mf})^{1/2}$, where K_u is the uniaxial magnetic anisotropy constant and A_{mf} is the intersublattice molecular field coefficient. The moderate spin-flop field is associated with the weak intersublattice interactions and the small magnetocrystalline anisotropy due to the isotropic $4f^7$ electron configuration (L = 0) of Eu^{2+} ions.

Theoretical Analysis of the Crystal and Electronic Structure and Exchange Constants. The lattice constants calculated for $EuMO_3$ (M = Ti, Zr, and Hf) are described in Table 4 along with those estimated based on the synchrotron XRD results. It should be noted that for $EuTiO_3$, the ratio of the lattice constants of the tetragonal supercell a to c remains 1 to $\sqrt{2}$ after the structural optimization and the lattice constant of $EuTiO_3$ is presented as $(a^2c/4)^{1/3}$; the tetragonal cell is hereafter referred to as a *cubic* model. The lattice constants

dx.doi.org/10.1021/ic2024567 | Inorg. Chem. 2012, 51, 4560–4567

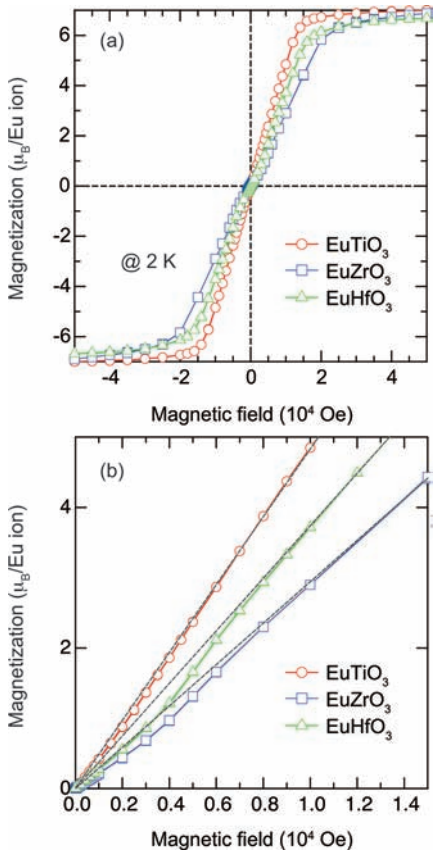

Figure 6. (a) Magnetic-field dependence of magnetization measured at 2 K for EuMO_3 (M = Ti, Zr, and Hf) and (b) the enlarged view of the low-field region. The dashed lines in (b) are guides to the eyes.

experimentally obtained are close to the values derived by the hybrid functional calculations although the experimental lattice constants were measured at room temperature. The difference between experimental and calculated lattice constants is less than 0.8% for all the compounds.

The G-type AFM configuration shows the lowest total energy among the four calculated magnetic configurations. The energy difference between the G-type AFM state and the next low-lying FM state is 0.22, 0.85, and 0.42 meV per formula unit for EuMO_3 with M = Ti, Zr, and Hf, respectively. The small difference in energy indicates that the G-type AFM and FM states are delicately balanced in the present compounds. The calculated exchange constants are shown in Table 4 along with those obtained by the analysis of the magnetic susceptibility. The calculations reproduce the experimental exchange constants well, although the absolute values of the calculated exchange constants as a whole are larger than those of the exchange constants obtained experimentally. The overestimation of exchange constants has also been found in previous hybrid Hartree−Fock density functional studies for other systems.[46]

Figure 7 shows the site-projected partial density of states and band structure for EuMO_3 (M = Ti, Zr, and Hf) with the G-type magnetic configuration. The valence band mainly consists of Eu 4f and O 2p states, while the conduction band chiefly has M nd and Eu 5d characters for EuMO_3 (M = Ti, Zr, and Hf and n = 3, 4, and 5, respectively). Occupied Eu 4f bands are considerably narrow, indicating that they are localized states. The band structures reveal that the conduction band bottom is located at the Γ point in the M nd bands for EuMO_3 (M = Ti, Zr, and Hf and n = 3, 4, and 5, respectively) while the valence

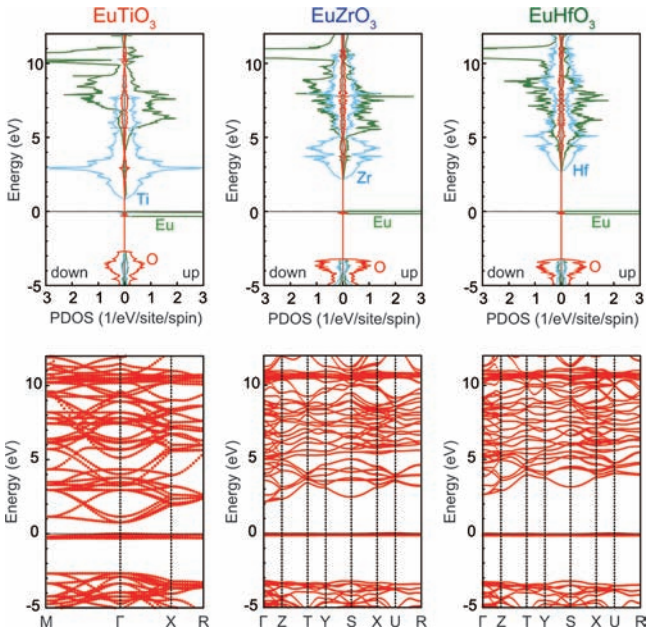

Figure 7. Site-projected partial density of states (PDOS) (top) and band structure for EuMO_3 (M = Ti, Zr, and Hf) with the G-type magnetic configuration. The PDOS of Eu is for an Eu site with up 4f spins. The zero of energy is placed at the highest occupied state.

Table 4. Comparison of Calculated and Experimental Values of Lattice Constants (a, b, and c), Band Gap (E_g), and Nearest-Neighbor (J_1) and Next-Nearest-Neighbor (J_2) Exchange Constants[a]

	a (Å)	b (Å)	c (Å)	E_g (eV)	J_1/k_B (K)	J_2/k_B (K)
			$EuTiO_3$			
calc.	3.903[b]			0.77	−0.009	0.076
exp.	3.90437(4)			0.8	−0.015	0.036
			$EuZrO_3$			
calc.	5.793	5.864	8.212	2.08	−0.048	0.025
exp.	5.79387(10)	5.82154(9)	8.19562(14)	2.4	−0.026	0.020
			$EuHfO_3$			
calc.	5.750	5.787	8.138	2.60	−0.024	0.032
exp.	5.77869(12)	5.79424(12)	8.16438(17)	2.7	−0.025	0.018

[a]The calculated values were obtained for the G-type magnetic configuration. [b]The ratio of the tetragonal lattice constants a to c for $EuTiO_3$ with the G-type magnetic configuration remains 1 to $\sqrt{2}$ after the structural optimization and, thereby, this value was obtained as $(a^2c/4)^{1/3}$.

dx.doi.org/10.1021/ic2024567 | Inorg. Chem. 2012, 51, 4560−4567

band top is positioned at the Γ point in the Eu 4f bands for $EuTiO_3$ and at the U point for $EuZrO_3$ and $EuHfO_3$. The band gap, which is estimated as the energy difference between the lowest unoccupied and highest occupied one-electron eigenstates, is summarized in Table 4. It is found that the hybrid functional calculations also provide band gaps which are in good agreement with those obtained from the diffuse reflectance spectroscopy. It should be noted that although the lowest-energy excitation is an indirect transition in $EuZrO_3$ and $EuHfO_3$, the difference between the direct and indirect transition energies is very small (<0.03 eV) because of the flatness of the Eu 4f bands. Because of its larger transition probability, the direct transition is considered to be predominant near the absorption edge in the optical spectra for $EuZrO_3$ and $EuHfO_3$. The difference in band gaps among $EuTiO_3$, $EuZrO_3$, and $EuHfO_3$ can be explained basically in terms of the energy levels of Ti 3d, Zr 4d, and Hf 5d states constituting the conduction bands of the corresponding compounds; the energy levels become higher with an increase in their principal quantum number, leading to the larger band gaps. Meanwhile, our calculations have revealed that the band gaps do not strongly depend on whether the cubic or orthorhombic structural model is employed, (data are not shown), so that the difference in band gaps can not be explained only by the structural difference.

In the present perovskites the magnetic interaction between the NN Eu^{2+} ions, J_1, is dominated by the AFM superexchange through the d states of the B-site cations as well as by the indirect FM exchange via the Eu 5d states, as revealed by the recent first-principles calculations.[28] The energy separation between the Eu 4f and M nd (M = Ti, Zr, and Hf and n = 3, 4, and 5, respectively) states, ΔE, corresponding to the band gap, strongly depends on the kind of M, while the energy difference between the Eu 4f and 5d states is almost independent of the kind of M. As ΔE increases, the AFM superexchange interaction through the M nd states should become weaker and make the absolute value of J_1 (<0) smaller, since a third-order perturbation energy of the superexchange interaction is represented as $J(t^2/\Delta E^2)$, where J and t are the exchange and transfer integral between the Eu 4f and M nd states, respectively. However, the variation of J_1 as listed in Table 4 can not be explained only by the difference of ΔE; one can see that the absolute values of J_1 for $EuZrO_3$ and $EuHfO_3$ are larger than that for $EuTiO_3$, despite the larger ΔE of the former two compounds. Here, it should be recalled that the calculations were performed using the cubic model without oxygen octahedral tilting ($a^0a^0a^0$) for $EuTiO_3$ (Figure 1a) and the orthorhombic models involving oxygen octahedral tilting ($a^-a^-c^+$) for $EuZrO_3$ and $EuHfO_3$ (Figure 1b). It has been revealed by our preliminary theoretical analysis that the tilting of MO_6 octahedra involved in the orthorhombic structure enhances the interaction between the Eu 4f and M nd states, leading to the stronger AFM superexchange interaction through the M nd states.[64] Thus, the magnetic interactions in $EuMO_3$ are intimately linked to both their crystal and electronic structures.

SUMMARY

A comparative study of the fundamental properties including the crystal and electronic structure and magnetic properties of divalent europium perovskites $EuMO_3$ (M = Ti, Zr, and Hf) has been performed based on experimental and computational approaches. $EuHfO_3$ has an orthorhombic structure very similar to that of $EuZrO_3$ at room temperature, in contrast to cubic $EuTiO_3$. $EuZrO_3$ and $EuHfO_3$ have band gaps of 2.4 and 2.7 eV, respectively, which are much larger than that of $EuTiO_3$. Despite such dissimilarities, the present compounds exhibit similar magnetic properties: AFM transitions at around 5 K and the AFM NN and FM NNN interactions. Spin-flop transitions are observed at 2 K under moderate magnetic fields lower than 1 T, implying relatively weak AFM NN interactions and small magnetic anisotropy, which are characteristic of the present compounds. The lattice constants, magnetic ground states, and band gaps experimentally observed are well reproduced by hybrid Hartree−Fock density functional calculations. Calculated partial density of states (PDOS) and band structures have revealed that the observed optical transitions near the absorption edge mainly stem from the direct-allowed charge-transfer transitions from the localized Eu 4f bands to the M nd bands for $EuMO_3$ (M = Ti, Zr, and Hf and n = 3, 4, and 5, respectively). Thus, our combined experimental and theoretical study provides a systematic understanding of the fundamental properties of the divalent europium perovskites.

AUTHOR INFORMATION

Corresponding Author

*E-mail: hirofumi.akamatsu@kt4.ecs.kyoto-u.ac.jp (H.A.), fujita@dipole7.kyoto-u.ac.jp (K.F.).

Notes

The authors declare no competing financial interest.

ACKNOWLEDGMENTS

The authors thank M. Tosaki and Y. Isozumi of Radioisotope Research Center, Kyoto University, for the Mössbauer effect measurements. The synchrotron powder XRD experiments were performed at the SPring-8 with the approval of the JASRI (Proposal Nos. 2011A1641 and 2011B1504). The authors appreciate J. E. Kim and N. Tsuji for their experimental support. This research was supported by Grants-in-Aid for Scientific Research on Priority Areas (No. 474) and (B) (No. 22360273), Challenging Exploratory Research (No. 23655198), and Young Scientists (A) (No. 23686089) from MEXT and for JSPS Fellows (No. 22-1280) from JSPS.

REFERENCES

(1) Ishikawa, K.; Adachi, G.; Shiokawa, J. *Mater. Res. Bull.* **1981**, *16*, 419−427.
(2) Katsufuji, T.; Tokura, Y. *Phys. Rev. B* **1999**, *60*, R15021.
(3) Katsufuji, T.; Takagi, H. *Phys. Rev. B* **2001**, *64*, 054415.
(4) Wu, H.; Jiang, Q.; Shen, W. Z. *Phys. Rev. B* **2004**, *69*, 014104.
(5) Fennie, C. J.; Rabe, K. M. *Phys. Rev. Lett.* **2006**, *97*, 267602-.
(6) Takahashi, K. S.; Onoda, M.; Kawasaki, M.; Nagaosa, N.; Tokura, Y. *Phys. Rev. Lett.* **2009**, *103*, 057204.
(7) Goian, V.; Kamba, S.; Hlinka, J.; Vanek, P.; Belik, A. A.; Kolodiazhnyi, T.; Petzelt, J. *Eur. Phys. J. B* **2009**, *71*, 429−433.
(8) Shvartsman, V. V.; Borisov, P.; Kleemann, W.; Kamba, S.; Katsufuji, T. *Phys. Rev. B* **2010**, *81*, 064426.
(9) Kolodiazhnyi, T.; Fujita, K.; Wang, L.; Zong, Y.; Tanaka, K.; Sakka, Y.; Takayama-Muromachi, E. *Appl. Phys. Lett.* **2010**, *96*, 252901.
(10) Rushchanskii, K. Z.; Kamba, S.; Goian, V.; Vanek, P.; Savinov, M.; Prokleska, J.; Nuzhnyy, D.; Knizek, K.; Laufek, F.; Eckel, S.; Lamoreaux, S. K.; Sushkov, A. O.; Lezaic, M.; Spaldin, N. A. *Nat. Mater.* **2010**, *9*, 649−654.
(11) Brous, J.; Fankuchen, I.; Banks, E. *Acta Crystallogr.* **1953**, *6*, 67−70.
(12) Shafer, M. W. *J. Appl. Phys.* **1965**, *36*, 1145−1152.
(13) McCarthy, G. J.; Greedan, J. E. *Inorg. Chem.* **1975**, *14*, 772−775.

(14) Viallet, V.; Marucco, J.-F.; Saint, J.; Herbst-Ghysel, M.; Dragoe, N. *J. Alloys Compd.* **2008**, *461*, 346−350.
(15) Zong, Y.; Fujita, K.; Akamatsu, H.; Murai, S.; Tanaka, K. *J. Solid State Chem.* **2010**, *183*, 168−172.
(16) Wei, T.; Liu, H.; Chen, Y.; Yan, H.; Liu, J.-M. *Appl. Surf. Sci.* **2011**, *257*, 4505−4509.
(17) Kugimiya, K.; Fujita, K.; Tanaka, K.; Hirao, K. *J. Magn. Magn. Mater.* **2007**, *310*, 2268−2270.
(18) Lee, J. H.; Ke, X.; Podraza, N. J.; Kourkoutis, L. F.; Heeg, T.; Roeckerath, M.; Freeland, J. W.; Fennie, C. J.; Schubert, J.; Muller, D. A.; Schiffer, P.; Schlom, D. G. *Appl. Phys. Lett.* **2009**, *94*, 212509.
(19) Fujita, K.; Wakasugi, N.; Murai, S.; Zong, Y.; Tanaka, K. *Appl. Phys. Lett.* **2009**, *94*, 062512−3.
(20) Hatabayashi, K.; Hitosugi, T.; Hirose, Y.; Cheng, X.; Shimada, T.; Hasegawa, T. *Jpn. J. Appl. Phys.* **2009**, *48*, 100208.
(21) Lee, J. H.; et al. *Nature* **2010**, *466*, 954−958.
(22) Momma, K.; Izumi, F. *J. Appl. Crystallogr.* **2008**, *41*, 653−658.
(23) McGuire, T. R.; Shafer, M. W.; Joenk, R. J.; Alperin, H. A.; Pickart, S. J. *J. Appl. Phys.* **1966**, *37*, 981−982.
(24) Ranjan, R.; Nabi, H. S.; Pentcheva, R. *J. Phys.: Condens. Matter* **2007**, *19*, 406217.
(25) Ranjan, R.; Nabi, H. S.; Pentcheva, R. *J. Appl. Phys.* **2009**, *105*, 053905−4.
(26) Goodenough, J. B. *Magnetism and the Chemical Bond*; Interscience: New York, 1963.
(27) Kasuya, T. *IBM J. Res. Dev.* **1970**, *14*, 214−223.
(28) Akamatsu, H.; Kumagai, Y.; Oba, F.; Fujita, K.; Murakami, H.; Tanaka, K.; Tanaka, I. *Phys. Rev. B* **2011**, *83*, 214421.
(29) Akamatsu, H.; Fujita, K.; Zong, Y.; Takemoto, N.; Murai, S.; Tanaka, K. *Phys. Rev. B* **2010**, *82*, 224403.
(30) Izumi, F.; Momma, K. *Solid State Phenom.* **2007**, *130*, 15−20.
(31) Blöchl, P. E. *Phys. Rev. B* **1994**, *50*, 17953−17979.
(32) Heyd, J.; Scuseria, G. E.; Ernzerhof, M. *J. Chem. Phys.* **2003**, *118*, 8207−8215.
(33) Heyd, J.; Scuseria, G. E.; Ernzerhof, M. *J. Chem. Phys.* **2006**, *124*, 219906.
(34) Krukau, A. V.; Vydrov, O. A.; Izmaylov, A. F.; Scuseria, G. E. *J. Chem. Phys.* **2006**, *125*, 224106.
(35) Kresse, G.; Hafner, J. *Phys. Rev. B* **1993**, *48*, 13115−13118.
(36) Kresse, G.; Furthmüller, J. *Phys. Rev. B* **1996**, *54*, 11169−11186.
(37) Kresse, G.; Joubert, D. *Phys. Rev. B* **1999**, *59*, 1758−1775.
(38) Paier, J.; Marsman, M.; Hummer, K.; Kresse, G.; Gerber, I. C.; Angyan, J. G. *J. Chem. Phys.* **2006**, *124*, 154709.
(39) Paier, J.; Marsman, M.; Hummer, K.; Kresse, G.; Gerber, I. C.; Angyan, J. G. *J. Chem. Phys.* **2006**, *125*, 249901.
(40) Perdew, J. P.; Burke, K.; Ernzerhof, M. *Phys. Rev. Lett.* **1996**, *77*, 3865−3868.
(41) Kudin, K. N.; Scuseria, G. E.; Martin, R. L. *Phys. Rev. Lett.* **2002**, *89*, 266402.
(42) Franchini, C.; Bayer, V.; Podloucky, R.; Paier, J.; Kresse, G. *Phys. Rev. B* **2005**, *72*, 045132.
(43) Oba, F.; Togo, A.; Tanaka, I.; Paier, J.; Kresse, G. *Phys. Rev. B* **2008**, *77*, 245202.
(44) Oba, F.; Togo, A.; Tanaka, I.; Watanabe, K.; Taniguchi, T. *Phys. Rev. B* **2010**, *81*, 075125.
(45) Oba, F.; Choi, M.; Togo, A.; Seko, A.; Tanaka, I. *J. Phys.: Condens. Matter* **2010**, *22*, 384211.
(46) Meyer, A.; Perger, W. F.; Demichelis, R.; B., C.; Dovesi, R. *Int. J. Quantum Chem.* **2010**, *110*, 2192−2201.
(47) Stroppa, A.; Marsman, M.; Kresse, G.; Picozzi, S. *New J. Phys.* **2010**, *12*, 093026.
(48) Marsman, M.; Paier, J.; Stroppa, A.; Kresse, G. *J. Phys.: Condens. Matter* **2008**, *20*, 064201.
(49) Wu, H.; Stroppa, A.; Sakong, S.; Picozzi, S.; Scheffler, M.; Kratzer, P. *Phys. Rev. Lett.* **2010**, *105*, 267203.
(50) Monkhorst, H. J.; Pack, J. D. *Phys. Rev. B* **1976**, *13*, 5188−5192.
(51) Chien, C.-L.; DeBenedetti, S.; Barros, F. D. S. *Phys. Rev. B* **1974**, *10*, 3913-.
(52) Ahtee, A.; Ahtee, M.; Glazer, A. M.; Hewat, A. W. *Acta Crystallogr. B* **1976**, *32*, 3243−3246.
(53) Guevara, J.; Cuffini, S.; Mascarenhas, Y.; Carbonio, R.; Alonso, J.; Fernandez, M.; De La Presa, P.; Ayala, A.; Lopez Garcia, A. *Mater. Sci. Forum* **1998**, *278*−*281*, 720−725.
(54) Shannon, R. D. *Acta Crystallogr. A* **1976**, *32*, 751−767.
(55) Glazer, A. M. *Acta Crystallogr. B* **1972**, *28*, 3384−3392.
(56) Bussmann-Holder, A.; Köhler, J.; Kremer, R. K.; Law, J. M. *Phys. Rev. B* **2011**, *83*, 212102.
(57) Bettis, J. L.; Whangbo, M.-H.; Köhler, J.; Bussmann-Holder, A.; Bishop, A. R. *Phys. Rev. B* **2011**, *84*, 184114.
(58) Müller, K. A. *Phys. Rev. Lett.* **1959**, *2*, 341−343.
(59) Shenoy, G.; Dunlap, B. *Nucl. Instrum. Methods* **1969**, *71*, 285−291.
(60) Fujita, K.; Tanaka, K.; Hirao, K.; Soga, N. *J. Am. Ceram. Soc.* **1998**, *81*, 1845-.
(61) Akamatsu, H.; Fujita, K.; Murai, S.; Tanaka, K. *Phys. Rev. B* **2010**, *81*, 014423.
(62) Misawa, Y.; Doi, Y.; Hinatsu, Y. *J. Solid State Chem.* **2011**, *184*, 1478−1483.
(63) Endo, T.; Doi, Y.; Wakeshima, M.; Hinatsu, Y. *Inorg. Chem.* **2010**, *49*, 10809−10814.
(64) Akamatsu, H.; Oba, F.; Kumagai, Y.; Fujita, K.; Tanaka, K.; Tanaka, I., unpublished work.